CHEMISTRY OF MATERIALS
ARTICLE
pubs.acs.org/cm

Composition-Tailored Synthesis of Gradient Transition Metal Precursor Particles for Lithium-Ion Battery Cathode Materials

Gary M. Koenig, Jr.,*[†] Ilias Belharouak,*[†] Haixai Deng,[†] Yang-Kook Sun,[‡] and Khalil Amine[†]

[†]Chemical Sciences and Engineering Division, Argonne National Laboratory, 9700 South Cass Avenue, Argonne, Illinois 60439, United States

[‡]Department of Chemical Engineering, Hanyang University, Seoul 133-791, South Korea

S *Supporting Information*

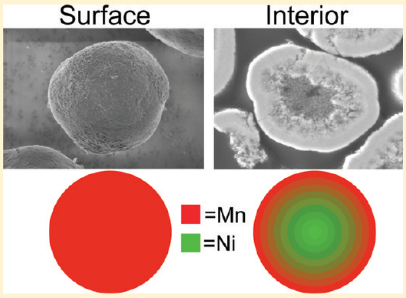

ABSTRACT: We report the tailored synthesis of particles with internal gradients in transition metal composition aided by the use of a general process model. Tailored synthesis of transition metal particles was achieved using a coprecipitation reaction with tunable control over the process conditions. Gradients in the internal composition of the particles was monitored and confirmed experimentally by analysis of particles collected during regularly timed intervals. Particles collected from the reactor at the end of the process were used as the precursor material for the solid-state synthesis of $Li_{1.2}(Mn_{0.62}Ni_{0.38})_{0.8}O_2$, which was electrochemically evaluated as the active cathode material in a lithium battery. The $Li_{1.2}(Mn_{0.62}Ni_{0.38})_{0.8}O_2$ material was the first example of a structurally integrated multiphase material with a tailored internal gradient in relative transition metal composition as the active cathode material in a lithium-ion battery. We believe our general synthesis strategy may be applied to produce a variety of new cathode materials with tunable interior, surface, and overall relative transition metal compositions.

KEYWORDS: gradient materials, cathode, tailored synthesis, transition metal oxide, lithium-ion battery

INTRODUCTION

Lithium-ion batteries are commonly used for energy storage in consumer electronics devices.[1,2] The pressures of increasing global energy demand, fluctuations in crude oil prices, and environmental concerns have increased attention on lithium-ion batteries for other applications that have greater energy demands, such as electric grid energy storage and plug-in hybrid electric and electric vehicles.[1−3] These new applications for lithium-ion batteries require materials that provide high capacities, high power, excellent safety and thermal stability, long calendar life, low cost, and low toxicity.[3] Efforts to meet these objectives have initiated research into new materials to replace the currently most common cathode material, $LiCoO_2$. In particular, a variety of materials have been developed to substitute all or some of the cobalt with other transition metals, especially nickel and manganese.[4−7] Ni and Mn are less expensive[8] and less toxic than Co,[9] and a variety of lithium transition metal oxides have been reported that have substituted all or most of the Co with Ni or Mn, including $LiMnO_2$,[4] $LiNiO_2$,[5] $Li(Ni_{0.5}Mn_{0.5})O_2$,[6] and $LiCo_{1/3}Ni_{1/3}Mn_{1/3}O_2$.[7] Some of these materials have also been reported to outperform $LiCoO_2$ with respect to rate capability[6] and capacity.[10]

A variety of oxides of lithium, Ni, and Mn have been investigated in efforts to produce desirable cathode materials.[4−7,10−19] High capacities have been reported for nickel-enriched materials;[11] however, these materials have suffered from poor cycle life and high interfacial cell impedance attributed to oxygen release and high concentrations of unstable Ni^{4+} ions.[12,13] Relatively lower capacities have been reported for manganese-enriched materials, but these materials have demonstrated excellent cycle life and safety attributed to their stability when in contact with the battery electrolyte.[6,14,15] Previous efforts have attempted to combine these two attributes, high stability with high capacity, by engineering cathode particles with a core enriched in Ni for high capacity and a shell enriched in Mn for high stability and cycling performance (so-called "core-shell" materials).[16−18] More recently, concerns over Li^+ diffusion across the core−shell interface within these cathode particles, and voids observed between the structurally and chemically distinct core and shell regions, led to a new particle design where a shell with a gradient in chemical composition was grown onto the surface of a core material which had a constant chemical composition.[10,19] Herein, we describe the synthesis of particles that have a core enriched in Ni and a surface enriched in Mn that differ from these previously reported materials by: (1) tailoring the composition of the precursor particles by modeling the concentration of the feed that entered a coprecipitation reactor and implementing this model in our process, and (2) synthesizing precursor particles that have a gradient in composition throughout the particle, as opposed to only within the shell region. We collected particles at multiple time points to follow the synthesis process, and performed a thorough characterization of the resulting multicomponent precursor materials. We also report the electrochemical characterization

Received: January 7, 2011
Published: March 09, 2011

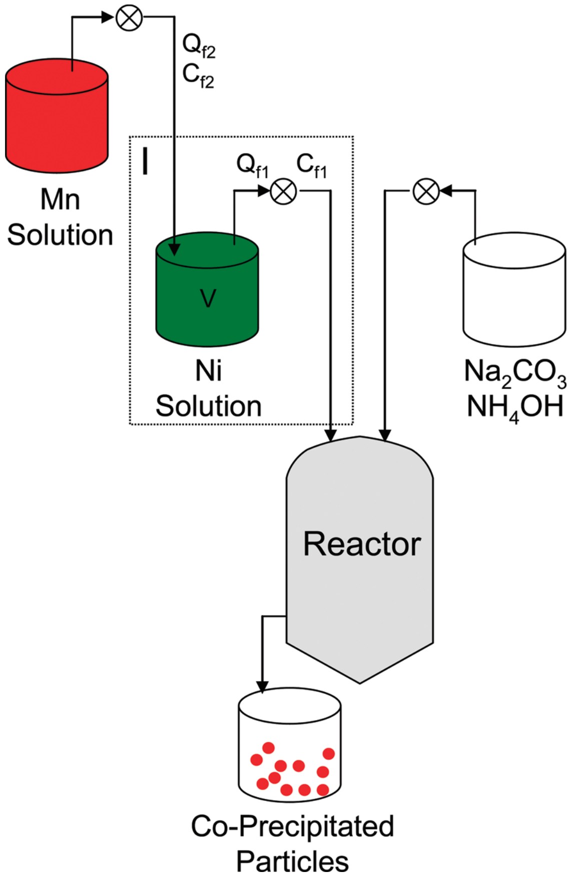

Figure 1. Illustration of the coprecipitation process.

of one of the lithiated final materials as the active cathode component in a lithium-ion cell.

MATERIALS AND METHODS

In an effort to tailor the gradient in our synthesized materials, we developed a model of our process to predict the relative concentration of transition metals that comprised our particles. For synthesizing our particles, we used a coprecipitation process schematically illustrated in Figure 1. As can be seen in Figure 1, a solution with a high composition of Mn ("Mn solution") was fed to a solution with a high composition of Ni ("Ni solution"), which was then fed to the reactor. The reactor was fed a solution that became enriched in Mn and reduced in Ni as a function of time, thus we expected the particles grown in the reactor would have cores enriched in Ni (deposited at earlier times) and surfaces enriched in Mn (deposited at later times). For these particles, the transition metal composition at the surfaces of the particles at any given time in the reactor should be approximately the same as the composition of the transition metals fed to the reactor at that given time. Assuming the material fed to the reactor deposited on the particle surfaces sequentially, tuning of the gradient and overall relative composition of transition metals within the particles was also possible. We tailored the overall composition of the particles, the gradient of the composition within the particles, and the transition metal composition at the surfaces of the particles by combining well-controlled process conditions with a model that predicted how these process conditions contributed to the composition of the transition metal feed that entered the reactor.

Calculation of the concentration of transition metals fed to the reactor was done by performing an input-output molar balance[20] on area "I" labeled in Figure 1. The variables are defined as follows:

Q_{f1} — Flow rate of feed to the reactor
C_{f1} — Concentration of a species in the feed to the reactor
Q_{f2} — Flow rate of Mn solution to Ni solution
C_{f2} — Concentration of a species in the Mn solution
V — Total volume of the solution that fed to the reactor (Ni solution)
V_i — Initial volume of the solution that fed to the reactor (Ni solution)
C_{f1i} — Initial concentration of solution fed to the reactor (Ni solution)
t - time

A molar balance on the Ni solution (area "I") as a function of time resulted in the following expression:

$$\frac{d(C_{f1}V)}{dt} = Q_{f2}C_{f2} - Q_{f1}C_{f1} \tag{1}$$

Applying the product rule to the left-hand side of eq 1, making appropriate substitutions for the volume, where $V = V_i + (Q_{f2} - Q_{f1})t$, and rearrangement of variables resulted in the following expression:

$$\frac{dC_{f1}}{dt} = \frac{Q_{f2}C_{f2} - Q_{f1}C_{f1}}{V_i + (Q_{f2} - Q_{f1})t} \tag{2}$$

The variables Q_{f1}, Q_{f2}, and C_{f2} were all known and well-controlled conditions in our process. At the start of the process ($t = 0$), $V = V_i$ and $C_{f1} = C_{f1i}$; and the initial volume and concentration of the Ni solution were also known and controlled process parameters.

Equation 2 was solved numerically to determine the concentration of any species fed to the reactor as a function of time. Because the concentration of the transition metals fed to the reactor directly reflected the concentration of the material deposited on the particles, solving the concentration profile of the feed to the reactor as a function of time enabled control and prediction of the gradient in the concentration of the resultant particles collected from the CSTR. As a proof-of-principle application of our model to the synthesis of gradient particles using our process, we chose operating conditions that (1) produced a gradient in concentration of transition metals within the particles from the beginning of the process, (2) resulted in a composition gradient that was deposited during an extended portion of the overall process, and (3) resulted in particles with surfaces that had greater relative concentrations of Mn than Ni. We wanted to produce a gradient in composition from the start of the process to investigate the feasibility of synthesizing particles with gradients in composition throughout entire particles. A continuous gradient could potentially help to mitigate separation that can occur between two chemically distinct regions within particles.[16,17] We wanted a gradient that was deposited during an extended amount of the process to easily track and confirm the deposition of the concentration gradient on collected particles. We collected particles in hour increments to track the chemical composition of the particles, both overall and at the surface, as a function of time. We wanted the surface enriched in Mn to avoid the cycling and safety problems that have been reported for lithium-ion batteries with cathode materials that had surfaces enriched in Ni.[12,13]

Precursor particles were produced via a coprecipitation process schematically illustrated in Figure 1. At the start of the process, a Ni solution (total volume of 3.0 L) of 2.0 mol/L $NiSO_4 \cdot 6H_2O$ (Aldrich) dissolved in distilled water was fed to a continuously stirred tank reactor (CSTR) at a rate of 1.0 L/h. Also at the beginning of the process, a Mn solution (total volume of 3.0 L) of 2.0 mol/L $MnSO_4 \cdot H_2O$ (Aldrich) dissolved in distilled water was fed to the Ni solution at a rate of 1.0 L/h. The Mn solution had completely emptied into the Ni solution after 3.0 h, and the Ni solution was completely emptied into the reactor after 6.0 h, signaling the end of the process. A solution of 0.2 mol/L NH_4OH (from 5.0 N solution, Fluka) and 2.0 mol/L Na_2CO_3 (anhydrous, Aldrich) was fed to the CSTR at a rate (~1.0 L/h) such that the pH inside the reactor was maintained at a constant 8.0. The temperature in the CSTR was kept constant at 60 °C, and mixing was achieved inside the reactor by an impeller that was set at 500 rotations per minute.

Precipitated particles in aqueous solution were continuously removed from the CSTR, and particles were collected for each hour of the process (i.e., hour 0−1, hour 1−2, hour 2−3, hour 3−4, hour 4−5, hour 5−6, and hour 6; hour 6 was the material collected from inside the reactor after the entire 6 h duration). Each batch of particles was kept separate for analysis of the coprecipitation process as a function of time. The particles were washed many times with distilled water, filtered, and dried overnight at 100 °C. The relative transition metal composition of the particles was qualitatively determined by using energy-dispersive X-ray spectroscopy (EDXS) on both the particle surfaces and the internal cross-sections of particles. We determined the overall relative transition metal composition of the particles by using inductively coupled plasma (ICP) measurements. For electrochemical measurements using the particles as active cathode materials within lithium-ion batteries, the dried precursor particles collected from the reactor were mixed with the desired amount of Li_2CO_3 (Adrich), fired in a furnace at 600 °C for 15 h, and then fired at 900 °C for an additional 15 h (both furnace firings done in air).

Powder X-ray diffraction (XRD, Siemens D5000) was performed using CuKα radiation. For images of surface morphology and EDXS on particle surfaces, powders were spread on double-sided carbon tape and mounted on stubs for evaluation in a scanning electron microscope (SEM, Hitachi S-4700-II). EDXS and SEM images were taken on internal cross sections of particles by embedding the particles in a resin which was cross-sectioned with an ultramicrotome. Thermal gravimetric analysis (TGA, Nietzsch STA449F3) was performed on the particles with compressed air as the purge gas.

Electrochemical testing consisted of charge−discharge tests on 2032-type coin cells at 25 °C. The coin cells had a lithium metal negative electrode separated from the positive electrode by a porous polypropylene separator. The positive electrode was comprised of 80 wt % active material, 10 wt % acetylene black, and 10 wt % polyvinylidene difluoride (PVDF) binder coated on aluminum foil. The electrolyte was 1.2 mol/L $LiPF_6$ dissolved in 3:7 ethylene carbonate:ethyl methyl carbonate. Coin cells were assembled in a He-filled glovebox.

RESULTS AND DISCUSSION

The process conditions during the coprecipitation synthesis described above were used in eq 2 to solve for the composition of transition metals fed to the reactor as a function of time. In this manuscript, when we refer to transition metal composition, we are referring to the relative composition of only the transition metals. The only transition metals fed to the reactor were Ni and Mn, and the sum of the relative molar compositions of these two transition metals totaled 100% throughout the process. The calculated composition profile for the feed to the reactor over the 6 h of the synthesis process is shown in Figure 2A. Over the first 3 h of the process, the Mn solution was fed to the Ni solution, leading to a gradually increasing composition of Mn (from 0% to 63.2%) fed to the reactor and a concurrent decrease in the Ni concentration (from 100% to 36.8%) in the feed. After 3 h, the Mn solution had completely emptied, and the final 3.0 L of solution was fed to the reactor over the last 3 h of the process with a constant relative composition of the two transition metals. A cartoon illustrating the qualitatively expected surface and interior compositions of a particle collected from the reactor at the end of the coprecipitation process is shown in Figure 2B. We expected a surface that was enriched in Mn, and an interior with a composition that gradually changed from enriched in Ni in the core to enriched in Mn at the surface. We expected that there would be a relatively thick layer of constant transition metal composition from the surface to the interior because the final 3 h of feed to the reactor had a constant relative transition metal composition.

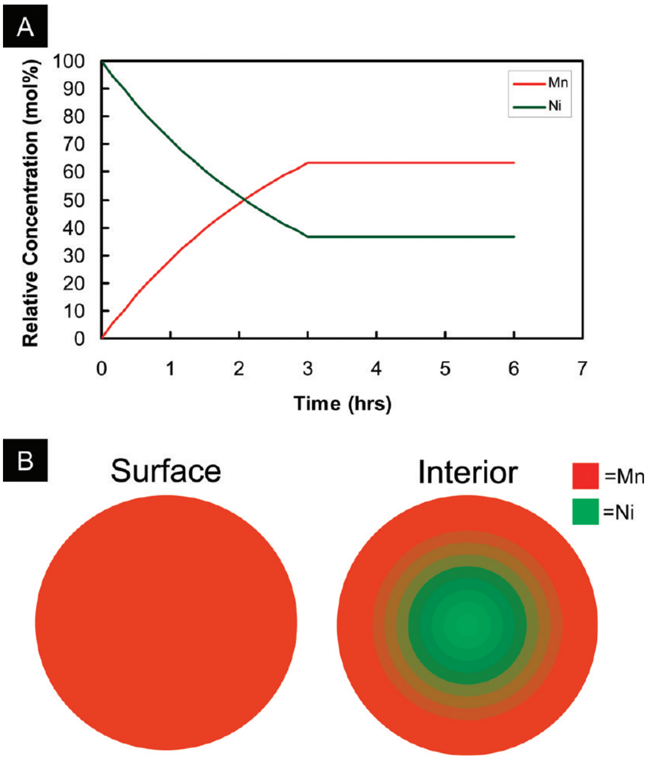

Figure 2. (A) Calculated concentration profile depicting the relative concentration of Mn and Ni fed to the reactor as a function of time. (B) Cartoon qualitatively illustrating the transition metal composition at the surface and interior of a particle formed with a continuous gradient in concentration from Ni-enriched in the center to Mn-enriched at the surface.

As mentioned above, we collected the coprecipitated particles in 1 h increments to investigate the growth of the gradient within the particles during the coprecipitation process. Figure 3 contains SEMs of the particles collected at the different time increments of the coprecipitation process. Figure 3A displays a particle from hour 0−1. During the first hour of the process, many of the particles were very small and formed asymmetric agglomerates after drying. The surfaces of the particles were rough and had many smaller particles that were loosely attached. Particles collected during hour 1−2 (Figure 3B) and hour 2−3 (Figure 3C) were progressively more symmetric and had noticeably less surface roughness. The surfaces of the particles continued to become smoother and the particle morphologies were more spherical as time progressed (Figure 3D). The particles collected during hour 4−5 (Figure 3E), hour 5−6 (Figure 3F), and hour 6 (Figure 3G) were very similar in appearance; they have very smooth surfaces relative to the particles collected at earlier times in the process and they were all approximately spherical in shape. The smooth, spherical particles collected from the reactor at the end of the process (Figure 3G) were similar to previous reports of smooth, spherical particles synthesized using carbonate coprecipitation of high Mn-concentration aqueous solutions.[21,22] SEM images of particles at lower magnification can be found in the Supporting Information (Figure S1).

In addition to imaging the surface morphologies of particles from the different collection times, we performed EDXS on the

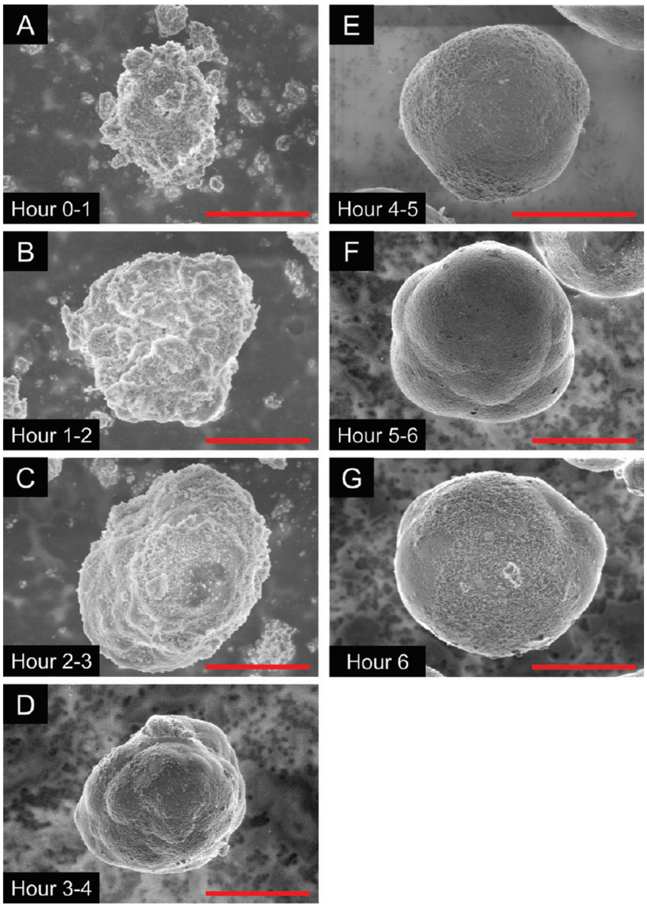

Figure 3. Representative SEMs of carbonate particles collected from the coprecipitation reactor during (A) hour 0−1, (B) hour 1−2, (C) hour 2−3, (D) hour 3−4, (E) hour 4−5, (F) hour 5−6, and (G) at the end of the 6 h process. Scale bars correspond to 10 μm.

surfaces of the collected particles to determine the approximate relative composition of the transition metals at the particle surfaces. The average relative Mn and Ni compositions were determined from EDXS measurements on multiple particles chosen at random from each collection time. The relative Mn composition (balance was Ni) as determined by EDXS on the surfaces of the particles as a function of the collection time can be found in Figure 4. We also calculated the average Mn concentration fed to the reactor for each collection time using the values calculated with eq 2 (e.g., for hour 0−1, we calculated the average Mn concentration fed to the reactor from the start of the process to the end of the first hour). For comparison, this calculated average relative concentration of Mn fed to the reactor as a function of collection time is also displayed in Figure 4. While EDXS measurements were approximate for these particles, if the transition metals fed to the reactor were deposited on the particles in the reactor sequentially, then we expected that the average relative transition metal composition of the feed to the reactor during a given collection time would be approximately the same as the measured relative composition of the transition metals at the surfaces of the particles collected during that same time. Both sets of data (Figure 4) have an increase in the relative composition of the Mn as the amount of time the process had been run increased. As can be seen in Figure 4, the agreement between the average relative Mn composition in the feed and the relative Mn composition measured at the surfaces of the particles was excellent for the last 2 collection times. For earlier collection times, however, the Mn composition measured at the surfaces of the particles was always less than the Mn composition fed to the reactor. One reason for the measured EDXS composition being lower than expected was that the interaction volume from EDXS was probing well below the particle surface.[23] Especially at early collection times, probing the volume below the particle surface meant that a volume was being probed which was leaner in Mn (and higher in Ni) than the Mn composition at the surface of the particle, resulting in a measured Mn composition which was lower than what was actually present at the particle surface. The reduction in the difference between the measured and calculated Mn composition from hour 3−4 to hour 6 was also consistent with the interaction volume influencing the measured surface composition, because during these collection times a constant Mn concentration was fed to the reactor. This period of constant feed concentration would build up a thicker and thicker layer on the particle of constant composition, which eventually would result in a shell of sufficient thickness to prevent the EDXS from picking up contributions from regions enriched in Ni below the constant composition shell. Although there was a significant offset between the measured and calculated Mn concentration at earlier time points, the increase in measured Mn concentration was much greater from hour 0−1 to hour 3−4 than it was from hour 3−4 to hour 6, which was consistent with the end of a gradient in the feed concentration after 3 h. The results presented above lead us to conclude that the increasing Mn concentration fed to the reactor coincided with increasing Mn concentrations at the surfaces of the collected particles.

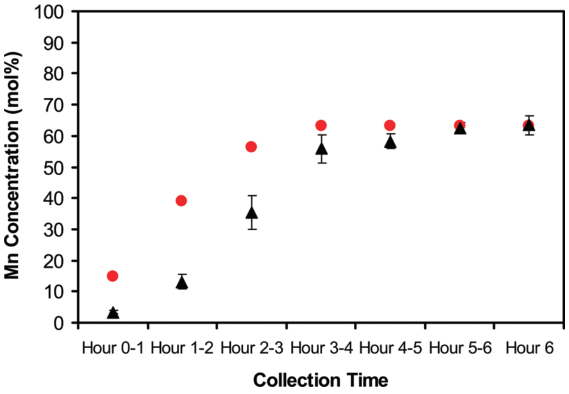

Figure 4. Relative average Mn concentration at the surfaces of the carbonate particles collected during different times in the coprecipitation process calculated (●) using eq 2 and measured using EDXS (▲).

The results presented above provide evidence that the relative transition metal concentration at the surfaces of the particles reflected the relative transition metal concentration in the feed to the reactor. To provide additional evidence that a material with a composition gradient from the core to the surface had been produced, we collected SEMs and EDXS data on the internal cross-sections of the particles. We separately analyzed the particles collected from hour 2−3 (Figure 5A), hour 4−5 (Figure 5B), and hour 6 (Figure 5C). The SEM in Figure 5A shows that for the particle collected from an early time in the coprecipitation process (hour 2−3), the particles had a more porous structure compared to the particles collected at the end of the process (Figure 5C). The internal cross-section reveals that

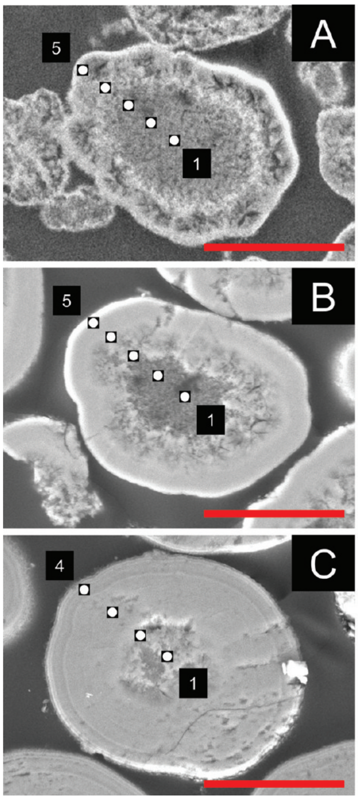

Point	%Mn
1	19.1
2	24.2
3	22.5
4	26.3
5	48.4

Point	%Mn
1	21.2
2	25.7
3	34.5
4	56.6
5	54.7

Point	%Mn
1	27.1
2	52.5
3	64.1
4	62.1

Figure 5. SEMs taken of the internal cross-section of particles collected from the reactor during (A) hour 2−3, (B) hour 4−5, and (C) at the end of 6 h. EDXS was performed at the labeled points 1 through 4 (or 5) from the core of the particle to the surface to determine the relative Mn composition at those locations. Scale bars correspond to 10 μm.

the particles collected during hour 2−3 had porous interiors in addition to rough and asymmetric surface morphologies (Figure 3C). Further insights into the internal porosity will be discussed below. EDXS spectra were collected from the points labeled 1 (center) through 5 (surface) in Figure 5A. The relative molar composition of Mn (balance Ni) is to the right of the image. The relative Mn composition increased from 19.1% in the center of the particle to 48.4% at the surface of the particle, indicating that there was a gradient in the Mn composition within this particle. We note that the gradient in composition does not appear to be very gradual, however, this may be in part due to dissolution/recrystallization of the material during the coprecipitation process.[24] The measured relative composition of Mn near the surface was 48.4%, which was greater than the composition measured using EDXS on the surfaces of whole particles (35.4%). This difference could be due to the increased relative contribution of the regions lean in Mn beneath the surfaces of the particles for the EDXS measured on the surfaces of whole particles.[23] The material collected during hour 4−5 (Figure 5B) also had a gradient in Mn composition, from 21.1% in the center to 54.7% near the surface. The relative Mn composition measured at the surfaces of whole particles was 58.2%, which was very close to this value. Not only does this particle have a gradient in transition metal composition but the SEM image of the particle (Figure 5B) reveals a noticeable morphological transition from more porous in the center to less porous near the surface of the particle. We hypothesize that less porous material enriched in Mn was sequentially deposited onto the surfaces of more porous particles that were formed earlier in the coprecipitation process. The particles collected after 6 h also have a composition gradient, from 27.1% Mn in the center to 62.1% Mn near the surface (Figure 5C). The relative Mn composition near the surface has excellent agreement with the composition measured on the surfaces of whole particles (63.5%). There was also a small porous core evident in the particles collected after 6 h (Figure 5C), which was noticeably smaller than the porous internal morphologies seen in particles collected during hour 2−3 (Figure 5A) and hour 4−5 (Figure 5C), providing additional evidence that a Mn-enriched dense material was deposited sequentially on the initially porous particles. EDXS and SEM analysis of the interiors and exteriors of particles lead us to conclude that a chemical and morphological gradient was sequentially deposited onto particles produced during the coprecipitation process.

In addition to SEM characterization, we performed X-ray diffraction (XRD) on particles harvested during different collection times to gain insights into the progression of the internal structure and overall composition of the materials formed during our process. Figure 6A shows an XRD pattern for particles collected during hour 0−1 of the coprecipitation. The XRD pattern was very broad; however, the majority of the features were consistent with the structure of $Ni(OH)_2 \cdot (NiOOH)_{0.167}$ ($R\bar{3}m$, ICSD #76650, reference positions indicated by green bars in Figure 6A).[25] This result indicated that early in the process, the Ni solution was primarily precipitated by OH^- ions in solution; however, as this synthesis was done in air, a mixture of hydroxides and oxyhydroxides was formed.[26] The main coprecipitating anion fed to the reactor during our process was CO_3^{2-}, thus the presence of Ni hydroxide/oxyhydroxide XRD features led us to speculate that the OH^- precipitation resulted from aqueous ammonia/ammonium hydroxide ($NH_4^+OH^-$) in solution, which produced the observed transition metal hydroxides/oxyhydroxides. During the next hour of the process, hour 1−2, the XRD pattern (Figure 6B) indicates that features from both $Ni(OH)_2 \cdot (NiOOH)_{0.167}$ (in green for reference) and one peak associated with $MnCO_3$ (ICSD #28556, $R\bar{3}c$, in red for reference)[25] was distinguishable. In particular, a pronounced peak at ∼11.5° was consistent with large spacing between $M(OH)_2$ slabs, which has been attributed in previous studies to the incorporation of anions to compensate for oxidation of the transition metals due to the synthesis being run in an air environment.[27] Figure 6B provides evidence that the particles collected during hour 1−2 contain $M(OH)_2$, MOOH, and MCO_3 (M = Mn, Ni), and likely some H_2O. The XRD pattern collected during hour 2−3 (Figure 6C) had relatively more pronounced $MnCO_3$-type features and less pronounced $Ni(OH)_2 \cdot (NiOOH)_{0.167}$-type features, providing evidence that the material from this collection time had increasingly more $MnCO_3$-type structure compared to the material collected earlier. The material collected from hour 3−4 (Figure 6D) only has the peak at ∼11.5° distinguishable as belonging to a $Ni(OH)_2 \cdot (NiOOH)_{0.167}$-type feature, with the $MnCO_3$-type features becoming increasingly dominant in the XRD pattern, indicating that most of the material formed a structure resembling a transition metal carbonate. The XRD patterns for particles collected during hour 4−5 (Figure 6E) have a very small feature remaining at ∼11.5° which indicated the decreasing abundance of $Ni(OH)_2 \cdot (NiOOH)_{0.167}$-type ordering within the material. The XRD patterns for the material collected during hour 5−6 (Figure 6F) and hour 6 (Figure 6G) were indistinguishable from

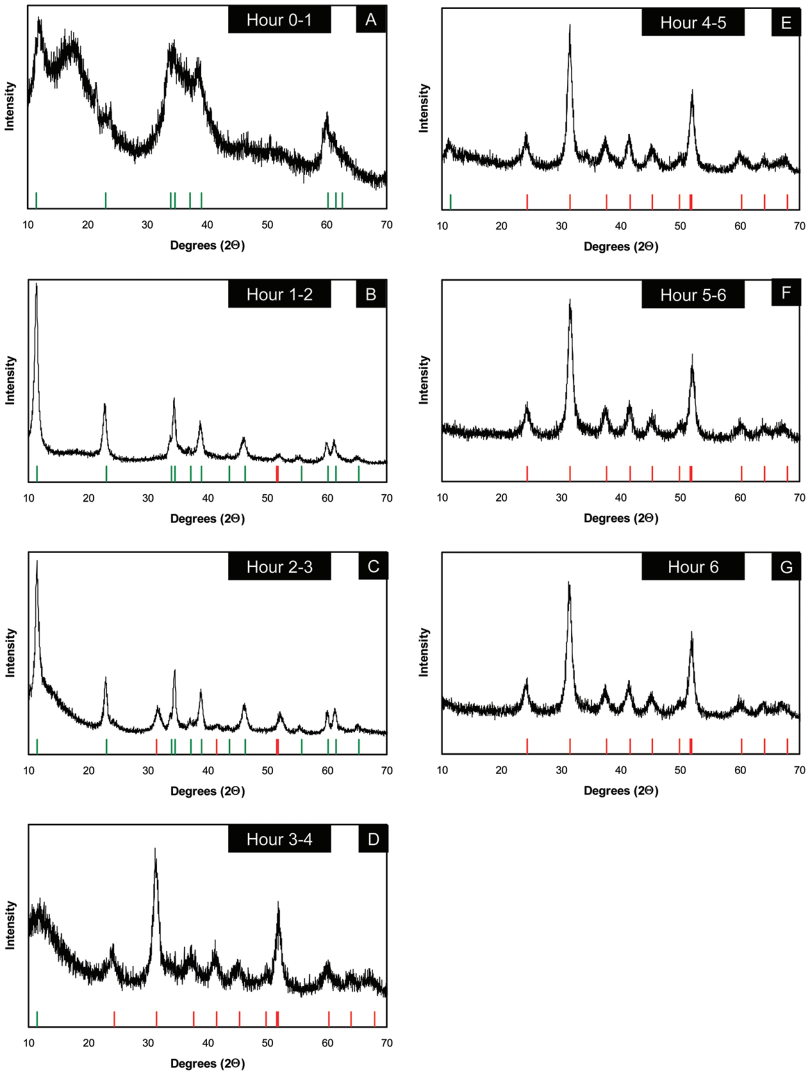

Figure 6. XRD patterns of carbonate particles collected during (A) hour 0−1, (B) hour 1−2, (C) hour 2−3, (D) hour 3−4, (E) hour 4−5, (F) hour 5−6, and (G) hour 6. Vertical green lines below the XRD patterns correspond to peak positions from a structure of $Ni(OH)_2 \cdot (NiOOH)_{0.167}$, whereas vertical red lines correspond to peak positions from a structure of $MnCO_3$.

each other, and features were no longer present that could be associated with a $Ni(OH)_2 \cdot (NiOOH)_{0.167}$ structure, indicating that any material within the particles that may have formed this structure was in too small a concentration to be detected in the XRD pattern. The final two XRD patterns have features consistent with a $MnCO_3$-type ordering within the material. The XRD patterns in Figure 6 are consistent with particles that were primarily precipitated metal hydroxides and oxyhydroxides early in the synthesis, contained an increasing amount of transition metal carbonate as the synthesis proceeded, and at the end of the process were primarily comprised of transition metal carbonate.

Thermal gravimetric analysis (TGA) was performed on the particles collected at different times during the synthesis to gain further insights into their chemical composition. All TGA profiles were collected in an air atmosphere. TGA profiles are shown for particles collected during hour 0−1 (Figure 7A), hour 2−3 (Figure 7B), hour 3−4 (Figure 7C), and hour 6 (Figure 7D). TGA data for hour 1−2, hour 4−5, and hour 5−6 can be found in the Supporting Information (Figure S2). For reference, we also ran TGA on commercially purchased $Ni(OH)_2$ (Aldrich, Figure 7E), $2NiCO_3 \cdot 3Ni(OH)_2 \cdot 4H_2O$ (Aldrich, Figure 7F), and $MnCO_3$ (Aldrich, Figure 7G). The particles collected during hour 0−1 (Figure 7A) have a gradual decrease in mass with increasing temperature up to ∼230 °C, followed by a sharp decrease in mass that reached a maximum in differential mass loss at ∼280 °C. The TGA profile for $Ni(OH)_2$ (Figure 7E) had only one noticeable loss in mass that occurred at ∼280 °C. These results, when combined, indicate that the particles collected during hour 0−1 have a significant amount of bound water that was gradually lost up to ∼230 °C, and that the most prevalent material was $Ni(OH)_2$, which decomposed most rapidly at ∼280 °C. As mentioned above, we speculate that the source of the hydroxide was OH^- ions from the aqueous ammonia/ammonium hydroxide fed to the reactor. The TGA profile for the particles collected during hour 2−3 (Figure 7B) had 4 distinguishable local maxima in the differential mass loss, at ∼130, ∼280, ∼520, and ∼790 °C. TGA performed on $2NiCO_3 \cdot 3Ni(OH)_2 \cdot 4H_2O$ (Figure 7F) had 2 local maxima at ∼130 and ∼310 °C, which we attribute to the loss of the bound water molecules in the structure (∼130 °C) and the decomposition of the hydroxide-carbonate species to form Ni oxide (∼310 °C). The TGA profile for $MnCO_3$ (Figure 7G) had a

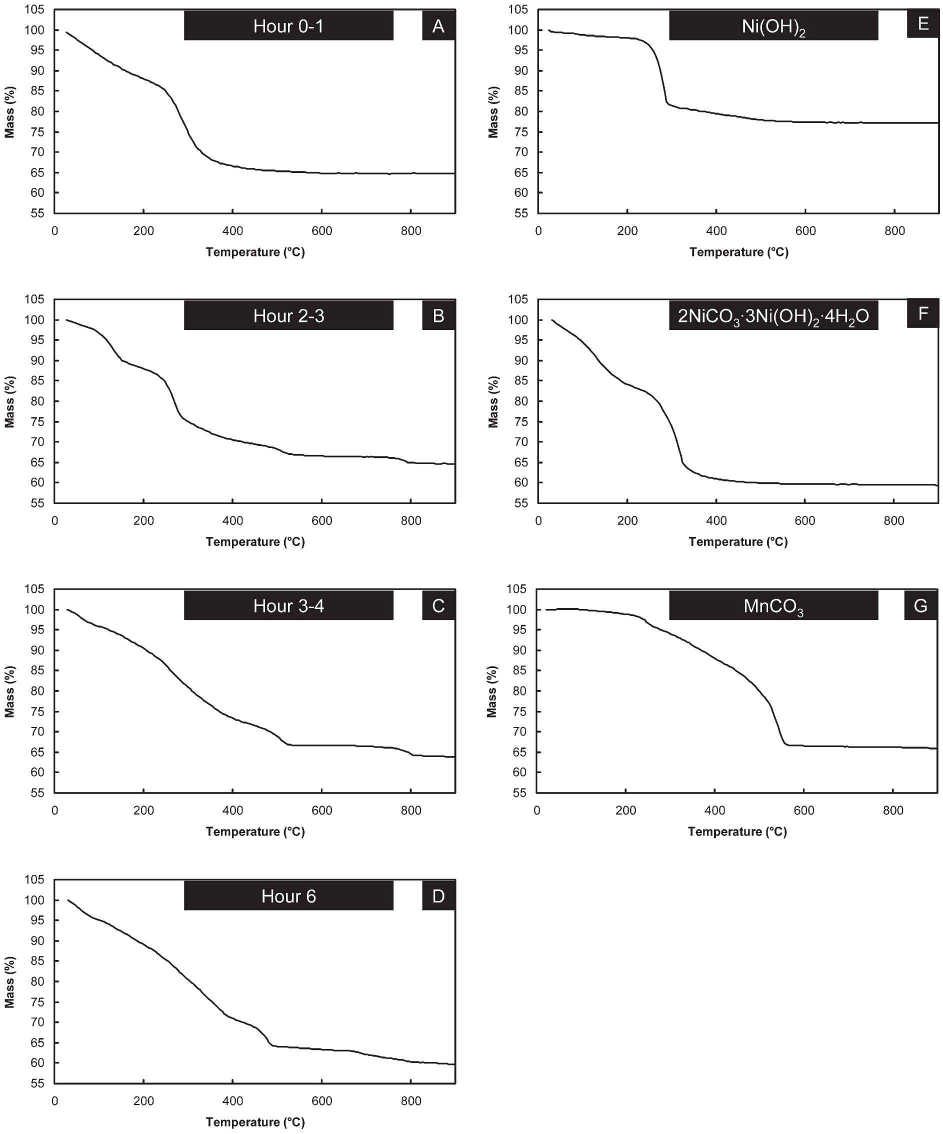

Figure 7. TGA profiles of carbonate particles collected during (A) hour 0−1, (B) hour 2−3, (C) hour 3−4, and (D) hour 6. TGA profiles are also shown for (E) $Ni(OH)_2$, (F) $2NiCO_3 \cdot 3Ni(OH)_2 \cdot 4H_2O$, and (G) $MnCO_3$.

gradual loss in mass that began at ~250 °C and had a local maximum at ~520 °C, which we attributed to the decomposition of the CO_3 species and the concurrent formation of Mn oxides. The TGA performed on the particles collected from hour 2−3 (Figure 7B) had features consistent with the presence of structural water such as that found in $2NiCO_3 \cdot 3Ni(OH)_2 \cdot 4H_2O$ (local maxima in differential mass loss at ~130 °C), $Ni(OH)_2$ (which led to the local maximum in differential mass loss at ~280 °C), and $MnCO_3$ (which resulted in the local maximum in differential mass loss at ~520 °C). The final feature in the TGA profile for the particles collected during hour 2−3 at ~790 °C was consistent with additional loss of oxygen from mixed Ni and Mn containing oxides within the material (e.g., $NiMnO_3 + Mn_2O_3 \rightarrow NiMn_2O_4 + 0.5\ Mn_2O_3 + 0.25\ O_2$).[21] This high temperature feature at ~790 °C was not present in the $Ni(OH)_2$ (Figure 7E), $2NiCO_3 \cdot 3Ni(OH)_2 \cdot 4H_2O$ (Figure 7F), or $MnCO_3$ (Figure 7G) samples because they only contain Ni or Mn, and this process required an oxide with a mixture of Ni and Mn.[21] Also, this feature was not seen for the particles collected during hour 0−1, indicating that there was insufficient Mn in this material to observe the high temperature decomposition reaction. The high temperature decomposition does take place with particles collected at later times, however, as the particles collected from hour 3−4 (Figure 7C) and hour 6 (Figure 7D) both have mass losses at ~790 °C. The particles collected during hour 3−4 (Figure 7C) and hour 6 (Figure 7D) have a gradual decomposition up to ~500 °C, however, the pronounced mass losses at ~130 °C and ~280 °C that were seen for the particles collected during hour 2−3 (Figure 7B) were not as prominent. This result indicated that there was less relative composition of $Ni(OH)_2$ and $2NiCO_3 \cdot 3Ni(OH)_2 \cdot 4H_2O$ in the materials collected later in the coprecipitation process. Also, the $MnCO_3$ decomposition feature at ~520 °C was more pronounced for the particles collected at later times, indicating increasing relative compositions of transition metal carbonates within particles collected at later times in the process. In summary, the TGA profiles in Figure 7 provide evidence that (1) the particles precipitated from

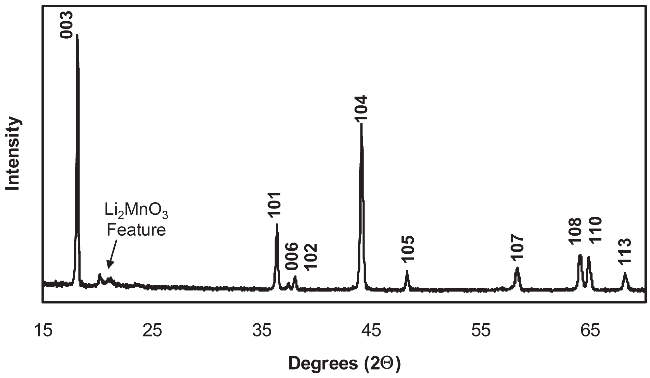

Figure 8. XRD pattern for $Li_{1.2}(Mn_{0.62}Ni_{0.38})_{0.8}O_2$.

our process were a mixture of structurally bound water, transition metal hydroxides/oxyhydroxides, and transition metal carbonates; and (2) the particles progressed from primarily $Ni(OH)_2$ at the beginning of the coprecipitation process to increasingly becoming a material that was enriched in $MnCO_3$. These observations were consistent with a coprecipitation process that produced a material that gradually increased the relative Mn composition and decreased the relative Ni composition of the resulting particles as a function of time.

After synthesizing and analyzing our coprecipitated precursor particles, we lithiated particles from the different collection times using various lithium-to-transition metal ratios to assess our materials' performance in lithium-ion battery cathodes. The detailed results of these studies will be reported in a future publication; however, here we report the structure, morphology, and electrochemical performance of one of our promising lithiated final materials. We performed ICP on the particles collected from the reactor (hour 6), and the overall relative molar transition metal composition was found to be 62% Mn and 38% Ni. The lithiated final material was produced with a composition of $Li_{1.2}(Mn_{0.62}Ni_{0.38})_{0.8}O_2$. The XRD pattern for the $Li_{1.2}(Mn_{0.62}Ni_{0.38})_{0.8}O_2$ material is shown in Figure 8. The pattern was indexed to the $R\bar{3}m$ structure (consistent with other $LiMn_xNi_{1-x}O_2$ structures, e.g., ICSD #28556),[25] although there were small features at 20−25° that were consistent with a Li_2MnO_3 integrated phase (e.g., ICSD #202639)[25] within the particles.[28,29] Features from the Li_2MnO_3-type phase, which adopts the $C2/m$ space group, have been reported for lithium transition metal oxides which were enriched in lithium and Mn, which was the case for our material.[28,29] Rietveld refinements were done on the XRD pattern using only the $R\bar{3}m$ space group, and lattice constants were calculated to be 2.852(7) Å for a and 14.214(0) Å for c, with a unit volume of 100.17 $Å^3$.[30] These values were comparable to those reported for lithium and Mn enriched layered transition metal oxides with fixed compositions (no composition gradients within individual particles).[29] XRD results indicated that the final lithiated material was primarily a layered transition metal oxide with a Li_2MnO_3-type integrated phase.

The surface and interior morphologies of the $Li_{1.2}(Mn_{0.62}Ni_{0.38})_{0.8}O_2$ material is shown in the SEMs in Figure 9. The final lithiated material particles were approximately spherical, and most particles were approximately 10−25 μm in diameter. Inspection of an individual particle SEM (Figure 9A) reveals that the size and shape of the precursor particles collected from the reactor (Figure 3G) were approximately retained during the lithiation process, however, larger primary particles were now found at the surfaces of the particles.[22,31,32] The internal particle morphology of the final lithiated material (Figure 9B) was also similar to the precursor material (Figure 5C). For both the precursor and final material, the particle morphology changes from more porous to more dense from the interior of the particle to the particle surface. There were large cracks present in the interior of the lithiated final material (Figure 9B), which may have resulted during the ultramicrotoming processing of the particle cross-sections. EDXS measurements performed at points on the cross-sectioned particle from the interior to the surface confirmed that a gradient in the transition metal composition was maintained after lithiatation/calcination. The relative Mn composition at the center of the particle was 37.3 mol % (balance Ni), whereas near the surface, the relative Mn composition was 61.6 mol %. The measured Mn concentration was slightly higher at the center of the particle and lower near the surface of the particle compared to the precursor material (Figure 5C), suggesting some redistribution of transition metals during the high-temperature lithiation process; however, a gradient in transition metal composition was maintained in the final material.

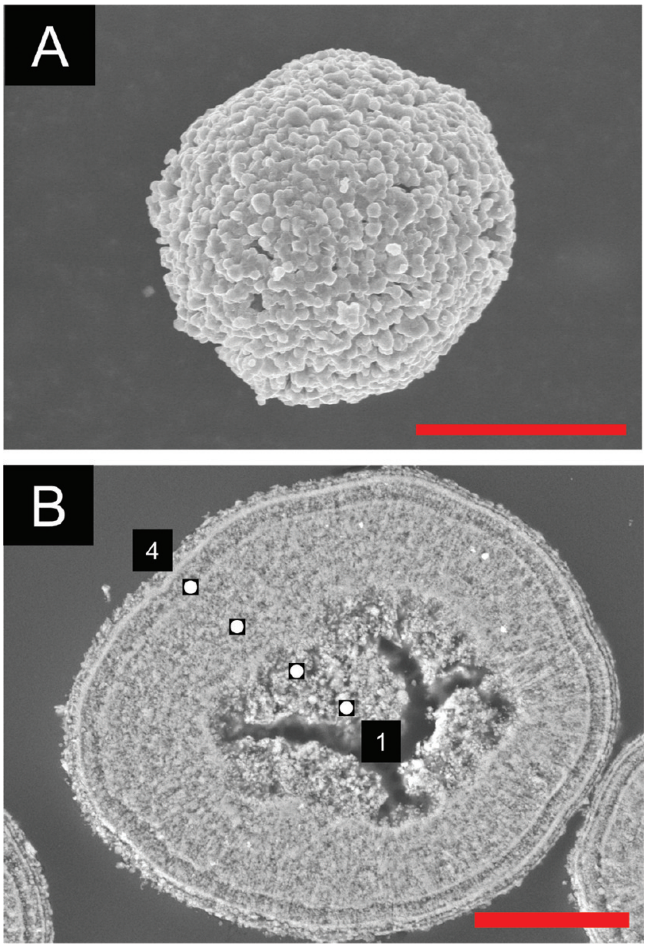

Figure 9. Scanning electron micrographs of (A) the surface and (B) the interior cross-section of a $Li_{1.2}(Mn_{0.62}Ni_{0.38})_{0.8}O_2$ particle. Scale bars correspond to (A) 10 and (B) 5 μm. The relative Mn composition as determined by EDXS on points 1−4 in (B) were 1, 37.3%Mn; 2, 55.2% Mn; 3, 62.2%Mn; 4, 61.6%Mn.

We evaluated the electrochemical performance of our $Li_{1.2}(Mn_{0.62}Ni_{0.38})_{0.8}O_2$ material as the cathode material in Li/

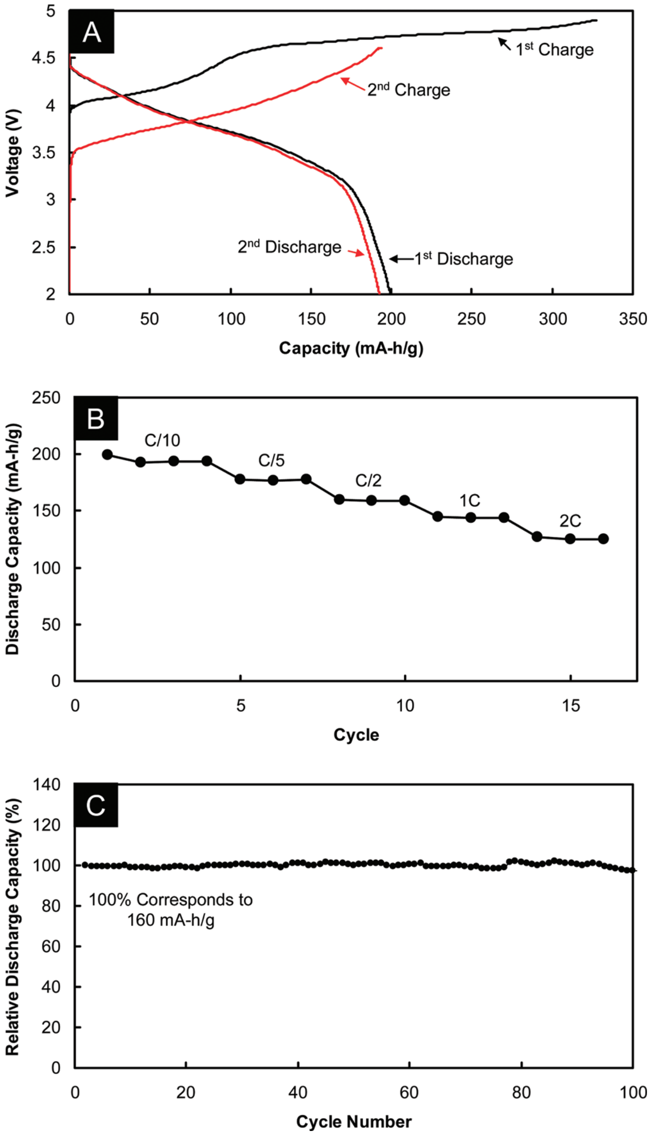

Figure 10. (A) First (black) and second (red) charge/discharge cycles for Li/$Li_{1.2}(Mn_{0.62}Ni_{0.38})_{0.8}O_2$ coin cells cycled at a rate of C/10 (1C corresponds to 200 mA/g). (B) Discharge capacity for Li/$Li_{1.2}(Mn_{0.62}Ni_{0.38})_{0.8}O_2$ coin cells cycled at increasing charging/discharging rates. (C) Relative discharge capacity of a Li/$Li_{1.2}(Mn_{0.62}Ni_{0.38})_{0.8}O_2$ coin cell during 100 cycles at a C/2 rate (100% corresponds to 160 mA h/g).

$Li_{1.2}(Mn_{0.62}Ni_{0.38})_{0.8}O_2$ coin cells. The coin cells were charged to 4.9 V at a rate of C/10 (1C corresponds to 200 mA/g), discharged to 2.0 V at C/10, and then cycled between 2.0 and 4.6 V at increasing rates for 3 cycles each at C/10, C/5, C/2, 1C, and 2C. The cells were charged during the first cycle to 4.9 V to activate the Li_2MnO_3 component within the composite material.[28,29] As can be seen in Figure 10A, there was a plateau during the first charge that began at ~4.5 V. Voltage plateaus in this region have previously been attributed to the extraction of lithium and/or oxygen from the Li_2MnO_3 component of the active material.[28,29] This process was irreversible, however, as confirmed by the dramatic reduction in charging capacity during the second charging cycle (194 mA h/g) compared to the first charging cycle (327 mA h/g), and by the absence of a plateau region beginning at ~4.5 V during the second charging of the material. Similar charge/discharge behavior for the first two cycles described above has been reported for materials that were enriched in lithium and Mn;[28,29] however, this is the first report of such profiles for precursor particles synthesized with a gradient in transition metal composition.

The capacity of Li/$Li_{1.2}(Mn_{0.62}Ni_{0.38})_{0.8}O_2$ coin cells at charge/discharge rates of C/10, C/5, C/2, 1C, and 2C are shown in Figure 10B. Capacity fade at increasing rates has been documented for $LiMO_2$-type materials (M = transition metal), and our $Li_{1.2}(Mn_{0.62}Ni_{0.38})_{0.8}O_2$ material had an average discharge capacity of 144 mA-h/g at 1C, compared with 193 mA-h/g at C/10.[33−35] Our material showed excellent capacity retention on cycling (Figure 10C). After first charging to 4.9 V and discharging to 2.0 V at a rate of C/10, we cycled our material for 100 charge/discharge cycles between 2.0 and 4.6 V at a rate of C/2. Relative to the first cycle at a rate of C/2, the Li/$Li_{1.2}(Mn_{0.62}Ni_{0.38})_{0.8}O_2$ coin cell retained 100% of its capacity after 50 cycles and 97% of its capacity after 100 cycles. While it was tempting to attribute the capacity retention to the Mn-enriched surfaces of the particles, we are currently in the process of evaluating the electrochemical performance of lithiated particles collected at different collection times during the coprecipitation process to evaluate the influence of the transition metal surface composition on the capacity retention during cycling. These results go beyond the scope of this manuscript, and they will be reported in a future publication.

CONCLUSIONS

A model and synthesis were described for producing particles via a coprecipitation process with tailored interior gradients in transition metal composition. Tailoring of the internal and surface composition of the particles was confirmed by SEM and EDXS analysis on both the surfaces and the interiors of particles collected during different times from the coprecipitation process. In addition to changes in transition metal composition, the particles were found to undergo changes in internal and external morphology and internal structure as a function of time. The particles collected from the reactor at the end of the coprecipitation process were lithiated to produce a lithium and Mn enriched $Li_{1.2}(Mn_{0.62}Ni_{0.38})_{0.8}O_2$ material. This lithiated final material was also confirmed to have a gradient in the internal relative transition metal composition from the core to the surface of the particles. The $Li_{1.2}(Mn_{0.62}Ni_{0.38})_{0.8}O_2$ material has an integrated Li_2MnO_3-type phase within the layered $R\bar{3}m$ structure. The material was evaluated electrochemically as the active cathode material for lithium-ion batteries in a Li/$Li_{1.2}(Mn_{0.62}Ni_{0.38})_{0.8}O_2$ coin cell and was found to have excellent retention of discharge capacity for the first 100 cycles. This is the first report of a structurally heterogeneous composite material produced from a precursor particle with a gradient in its internal composition. We have presented a general method that can be extended to create a new family of materials with tunable transition metal compositions, both within the particle interiors and at the surfaces of the particles, for lithium-ion battery cathodes.

ASSOCIATED CONTENT

Ⓢ Supporting Information. SEM images on whole particles at low magnification for each collection time, and additional

TGA data (PDF). This material is available free of charge via the Internet at http://pubs.acs.org.

AUTHOR INFORMATION

Corresponding Author

*Tel: 630-252-4450. Fax: 630-252-4671. Email: gkoenig@anl.gov (G.M.K.); belharouak@anl.gov (I.B.).

ACKNOWLEDGMENT

This research was funded by the U.S. Department of Energy, FreedomCAR, and Vehicle Technologies Office. We acknowledge Dr. Nancy L. Dietz Rago for SEM and EDXS analysis of particle cross-sections, and Dr. Huiming M. Wu for helpful discussions. Some electron microscopy was accomplished at the Electron Microscopy Center for Materials Research at Argonne National Laboratory, a U.S. Department of Energy Office of Science Laboratory. Argonne National Laboratory is operated for the U.S. Department of Energy by UChicago Argonne, LLC, under contract DE-ACOZ-06CH11357.

REFERENCES

(1) Armand, M.; Tarascon, J.-M. *Nature* **2008**, *451*, 652.

(2) Scrosati, B.; Garche, J. *J. Power Sources* **2010**, *195*, 2419.

(3) Goodenough, J. B.; Kim, Y. *Chem. Mater.* **2010**, *22*, 587.

(4) Armstrong, A. R.; Bruce, P. G. *Nature* **1996**, *6*, 499.

(5) Li, W.; Reimers, J. N.; Dahn, J. R. *Solid State Ionics* **1993**, *67*, 123.

(6) Kang, K.; Meng, Y. S.; Breger, J.; Grey, C. P.; Ceder, G. *Science* **2006**, *311*, 977.

(7) Ohzuku, T.; Makemura, Y. *Chem. Lett.* **2001**, *30*, 642.

(8) www.metalprices.com September 2010.

(9) http://www.atsdr.cdc.gov/cercla/; CERCLA Priority List of Hazardous Substances.

(10) Sun, Y.-K.; Myung, S.-T.; Park, B.-C.; Prakash, J.; Belharouak, I.; Amine, K. *Nat. Mater.* **2009**, *8*, 320.

(11) Kim, M.-H.; Shin, H.-S.; Shin, D.; Sun, Y.-K. *J. Power Sources* **2006**, *159*, 1328.

(12) Shim, J.; Kostecki, R.; Richardson, T.; Song, X.; Striebel, K. A. *J. Power Sources* **2002**, *112*, 222.

(13) Belharouak, I.; Lu, W.; Vissers, D.; Amine, K. *Electrocem. Comm.* **2006**, *8*, 329.

(14) Deng, H.; Belharouak, I.; Wu, H.; Dambournet, D.; Amine, K. *J. Electrochem. Soc.* **2010**, *157*, A776.

(15) Yoon, W.-S.; Paik, Y.; Yang, X.-Q.; Balasubramanian, M.; McBreen, J.; Grey, C. P. *Electrochem. Solid-State Lett.* **2002**, *5*, A263.

(16) Sun, Y.-K.; Myung, S.-T.; Kim, M.-H.; Prakash, J.; Amine, K. *J. Am. Chem. Soc.* **2005**, *127*, 13411.

(17) Sun, Y.-K.; Myung, S.-T.; Park, B.-C.; Amine, K. *Chem. Mater.* **2006**, *18*, 5159.

(18) Sun, Y.-K.; Myung, S.-T.; Shin, H.-S.; Bae, Y. C.; Yoon, C. S. *J. Phys. Chem. B* **2006**, *110*, 6810.

(19) Sun, Y.-K.; Kim, D.-H.; Yoon, C. S.; Myung, S.-T.; Prakash, J.; Amine, K. *Adv. Funct. Mater.* **2010**, *20*, 485.

(20) Rawlings, J. B.; Ekerdt, J. G. *Chemical Reactor Analysis and Design Fundamentals*; Nob Hill Publishing: Madison, WI, 2002.

(21) Deng, H.; Belharouak, I.; Sun, Y.-K.; Amine, K. *J. Mater. Chem.* **2009**, *19*, 4510.

(22) Park, S.-H.; Kang, S.-H.; Belharouak, I.; Sun, Y.-K.; Amine, K. *J. Power Sources* **2008**, *177*, 177.

(23) Goldstein, J.; Newbury, D.; Joy, D.; Lyman, C.; Echlin, P.; Lifshin, E.; Sawyer, L.; Michael, J. *Scanning Electron Microscopy and X-Ray Microanalysis*; Springer: New York, 2003.

(24) van Bommel, A.; Dahn, J. R. *Chem. Mater.* **2009**, *21*, 1500.

(25) *ICSD: The Inorganic Crystal Structure Database*; NIST: Gaithersburg, MD, 2010.

(26) van Bommel, A.; Dahn, J. R. *J. Electrochem. Soc.* **2009**, *156*, A362.

(27) Zhou, F.; Zhao, X.; Bommel, A. v.; Rowe, A. W.; Dahn, J. R. *Chem. Mater.* **2009**, *22*, 1015.

(28) Thackeray, M. M.; Johnson, C. S.; Vaughey, J. T.; Li, N.; Hackney, S. A. *J. Mater. Chem.* **2005**, *15*, 2257.

(29) Johnson, C. S.; Li, N.; Lefief, C.; Vaughey, J. T.; Thackeray, M. M. *Chem. Mater.* **2008**, *20*, 6095.

(30) Roisnel, T.; Rodriguez-Carvajal, J. *Fullprof Manual*; Institut Laue-Langevin: Grenoble, France, 2000.

(31) Kang, S.-H.; Park, S.-H.; Johnson, C. S.; Amine, K. *J. Electrochem. Soc.* **2007**, *154*, A268.

(32) Deng, H.; Belharouak, I.; Cook, R. E.; Wu, H.; Sun, Y.-K.; Amine, K. *J. Electrochem. Soc.* **2010**, *157*, A447.

(33) Oh, S. W.; Park, S.-H.; Amine, K.; Sun, Y.-K. *J. Power Sources* **2006**, *160*, 558.

(34) Xiao, J.; Chernova, N. A.; Whittingham, M. S. *Chem. Mater.* **2010**, *22*, 1180.

(35) Park, S.-H.; Shin, H.-S.; Myung, S.-T.; Yoon, C. S.; Amine, K.; Sun, Y.-K. *Chem. Mater.* **2005**, *17*, 6.